

# Structural and energetic differences between the human RXR $\alpha$ –PPAR $\gamma$ heterodimer with and without DNA binding

**Faizul Azam**

<sup>1</sup>Department of Pharmaceutical Chemistry and Pharmacognosy, Unaizah College of Pharmacy, Qassim University, Unaizah, 51911, Saudi Arabia <https://orcid.org/0000-0002-2927-8167>

**Martiniano Bello** (✉ [bellomartini@gmail.com](mailto:bellomartini@gmail.com))

<sup>2</sup>Laboratorio de Diseño y Desarrollo de Nuevos Fármacos e Innovación Biotecnológica, Escuela Superior de Medicina, Instituto Politécnico Nacional <https://orcid.org/0000-0002-9686-0755>

---

## Research Article

**Keywords:** RXR $\alpha$ , PPAR $\gamma$ , MD simulations, MMGBSA, binding free energy

**Posted Date:** June 6th, 2022

**DOI:** <https://doi.org/10.21203/rs.3.rs-1724133/v1>

**License:** © ⓘ This work is licensed under a Creative Commons Attribution 4.0 International License.

[Read Full License](#)

---

# Abstract

Structural data of multidomain structures of nuclear receptor complexes provides essential insights into how the quaternary complex impacts the nuclear receptor function. The heterodimeric complex between retinoic X receptor alpha (RXR $\alpha$ ) and peroxisome proliferator-activated receptor gamma (PPAR $\gamma$ ) is one of the most important and predominant regulatory systems, controlling lipid metabolism by binding to specific DNA promoter regions. X-ray and molecular dynamics (MD) simulations have revealed the average conformation adopted by the RXR $\alpha$ –PPAR $\gamma$  heterodimer bound to DNA, providing information about how multiple domains communicate to regulate receptor properties. However, knowledge of the energetic basis of the protein-ligand and protein-protein interactions is still lacking. Here we explore the structural and energetic mechanism of RXR $\alpha$ –PPAR $\gamma$ –DNA systems through microsecond MD simulations, molecular mechanics generalized Born surface area binding free energy calculations, principal component analysis, the free energy landscape, and correlated motion analysis. In our MD simulations, the RXR $\alpha$ –PPAR system was either bound or not bound to DNA and formed a complex with co-crystallized ligands (PDB entry 3DZY). Our results reveal new protein-ligand and protein-protein interactions that had not been reported in prior crystallographic studies. Binding free energy studies showed differences in protein-ligand and protein-protein affinity, whereas principal component analysis revealed differences in the conformational entropy depending on whether RXR $\alpha$ –PPAR $\gamma$  is bound or not bound to DNA. Correlated motions suggested that the allosteric communication is DNA dependent and bidirectional, impacting the protein-ligand and protein-protein interactions.

## 1. Introduction

Nuclear receptors (NRs) are a large group of multidomain proteins that regulate the transcription of numerous genes in humans by attaching to specific sequences and regulating gene expression [1–4]. Peroxisome proliferator-activated receptors (PPARs) are ligand-activated transcription factors belonging to the NR superfamily [5]. There are three subtypes of PPARs— $\alpha$ ,  $\gamma$ , and  $\delta$ —each with distinct tissue distribution [6–9]. PPAR $\gamma$  is found in the liver, kidney, muscle, adipose tissue, and heart, and it is essential in adipogenesis: Its overexpression enhances adipogenesis *in vitro* [10]. PPAR $\gamma$  plays a critical role in regulating glucose and lipid metabolism; therefore, it has been associated with diabetes, obesity, and cardiovascular diseases [11, 12]. Thiazolidinediones are a class of PPAR $\gamma$  ligands that improve insulin resistance by promoting adipocyte differentiation via PPAR $\gamma$  activation in adipocytes with a high capability to utilize glucose [13, 14]. Retinoic X receptors (RXRs) are also part of the NR superfamily and form obligate heterodimers with PPARs [15]. These receptors bind the vitamin A metabolite 9-*cis*-retinoic acid (9CR) [16]. There are three subtypes of RXRs— $\alpha$ ,  $\gamma$ , and  $\delta$ —which bind to DNA and activate transcription in response to 9CR homodimers. RXRs also form heterodimer complexes with other class 1 NRs, such as thyroid hormone, retinoic acid, and vitamin D receptors [17]. Some of the permissive RXR heterodimers are those formed with PPARs, so they can be activated by 9CRA. Modulating the permissive heterodimers by cognate ligands offers an additional level of regulation [17]. Topologically, these NRs consist of three major domains: (1) an N-terminal domain, also termed the A/B region; (2) a small, well-

conserved DNA binding domain (DBD) containing two zinc fingers that recognize specific DNA sequences, alongside a flexible hinge that connects the DBD to the ligand-binding domain (LBD); and (3) an LBD containing the activation function-2 (AF-2) surface at its C-terminus and a dimerization interface (Fig. 1) [18, 19]. The LBD of PPARs comprises 13  $\alpha$ -helices and four short  $\beta$ -strands [20]. Helices H2 and H3 form a very flexible loop localized at the entrance of the ligand-binding site [21]. The LBD of RXR $\alpha$  comprises 11  $\alpha$ -helices and two short  $\beta$ -strands [22]. The obligate RXR $\alpha$ –PPAR $\gamma$  heterodimer is one of the most important and predominant regulatory systems, regulating lipid metabolism by gene expression. The RXR $\alpha$ –PPAR $\gamma$  system regulates gene transcription by binding to specific DNA promoter regions [23]. In the holo state, H12 present in LBD in NRs is highly dynamic, taking on different conformations ranging from active to inactive. Upon ligand binding, the dynamics of H12 can be stabilized, altering the coregulator protein interaction surface, known as the AF-2 surface that comprises H3, loop<sub>H3–H4</sub>, H11, and H12 [24].

Structural data collected by X-ray crystallography, electron microscopy, and small-angle X-ray scattering (SAXS) have revealed that the binding of either a coactivator or a corepressor switches the heterodimer complex from the active to the inactive state. In the active state, the heterodimer is coupled to activating ligands, and the coactivators bind DNA and activate gene expression. In contrast, in the inactive state, the activating ligands and the coactivators are substituted by corepressors [25–27]. Recent evidence has shown that the structural mobility of LBDs is impacted by their interaction with DNA [28], and ligand-induced activation is dependent on the anchoring DNA sequence [29, 30]. Molecular dynamics (MD) simulations of the RXR $\alpha$ –PPAR $\delta$  heterodimer showed that the mobility of H10 and H11 (H10/11) of PPAR $\alpha$  is affected by RXR $\alpha$  ligand binding, indicating that these protein regions are involved in allosteric communication [31]. Amber-Vitos et al. performed MD simulations using active and modeled inactive RXR $\alpha$ –PPAR $\delta$ –DNA systems [32]. They found that in the forced inactive state, the two LBDs, the hinge region, and the two DBD regions are much more rigid. Recently, dynamic simulation in conjunction with analysis of correlated motions and using the active RXR $\alpha$ –PPAR $\gamma$ –DNA system identified distant correlated motions. Ricci et al. performed MD simulations and identified changes at the nanosecond timescale, namely a flux of correlated motions from DNA directed to the LBDs, mediated by the DBD of PPAR $\gamma$ , but without the participation of the RXR $\alpha$  DBD [33]. This finding aligns with hydrogen-deuterium exchange experiments using the vitamin D receptor (VDR)–RXR complex [28]. Although there has been support for communication between DBDs, LBDs, and DNA, this communication has also been observed in the non-permissive form of RXR–retinoic acid receptor (RAR) heterodimers [34]. These structural and MD simulations support the presence of synergism and communication between DBDs, LBDs, and DNA of the ternary RXR $\alpha$ –PPAR $\gamma$ –DNA system. Understanding these phenomena, together with an energetic study (still lacking), could increase knowledge about this system. In this study, we explore the structural and energetic basis of the active RXR $\alpha$ –PPAR $\gamma$ , and RXR $\alpha$ –PPAR $\gamma$ –DNA systems through triplicate microsecond MD simulations, followed by comparative analyses in terms of binding free energies using the molecular mechanics generalized Born surface area (MMGBSA) approach, principal component analysis (PCA), the free energy landscape (FEL), and correlated motion analyses. Our results shed light on

the dynamic and energetic aspects of the allosteric communication of the RXR $\alpha$ -PPAR $\gamma$  and RXR $\alpha$ -PPAR $\gamma$ -DNA systems.

## 2. Methods

### 2.1 Structural modeling

A missing portion of RXR $\alpha$  (residues 242–263) was constructed by using Modeller 9.17 [35]. The RXR $\alpha$  sequence was retrieved from Uniprot entry P19793 and chain A from PDB entry 3DZY chain A and added to the above-mentioned RXR $\alpha$  region. A missing protein region on PPAR $\gamma$  (residues 260–275) was constructed by using Modeller 9.17. The PPAR $\gamma$  isoform 1 sequence was retrieved from Uniprot entry P37231 and chain D from PDB entry 3DZY chain D and added to the above-mentioned PPAR $\gamma$  region. The model was constructed by using Modeller 9.17. The quality of the systems was evaluated with MolProbity [36].

### 2.2 MD simulations

The RXR $\alpha$ -PPAR $\gamma$ -DNA, and RXR $\alpha$ -PPAR $\gamma$  systems in which RXR $\alpha$  forms a complex with 9CR and PPAR $\gamma$  forms a complex with rosiglitazone (RGZ) were solvated with the TIP3P water model [37] in a periodic dodecahedron box with a solute-box wall distance of 1.5 nm. The net charges of each system were neutralized with Na<sup>+</sup> and Cl<sup>-</sup> counterions at the physiological concentration of 0.15 M. The protein, water molecules, and ions were specified by the ff14SB AMBER force field [38], and the DNA was specified by the ff99bsc0 + OL15 force field [39]. The ligand force field was built by designating AM1-BCC atomic charges using the general Amber force field (GAFF) [40]. The minimization and relaxing protocol consisted of 1,000 steps of energy minimization; 1000 ps of pre-relaxation with the protein-heavy and ligand atoms restrained; 1000 ps relaxation without restrictions on the ligand atoms; 1000 ps of relaxation with no restrictions to the side chains of the residues 5 Å around the ligand; and 1000 ps of NPT relaxation without restrictions for protein and ligand atoms. MD simulations consisted of three independent 1  $\mu$ s production simulations, each initialized with distinct initial atomic velocities determined from a Maxwell distribution at 310 K. In the production MD simulations, the SHAKE algorithm [41] was selected to restrain all bonds to equilibrium lengths, allowing a time step of 2 fs. The particle-mesh Ewald (PME) method [42] was used to treat the long-range electrostatic interactions with a cut-off of 1.0 nm. Van der Waals interactions were treated with the Verlet scheme with a cut-off distance of 1.0 nm. The system temperature was controlled at 310 K with a time constant of 0.1 ps, and the system pressure was kept at 1 atm.

### 2.3 MD trajectory analysis

For the triplicate MD simulations, the time-dependent Ca root-mean-squared deviation (RMSD), the radius of gyration (Rg), and clustering analysis were evaluated using AmberTools16. For each complex, the equilibrated part of each simulation was concatenated into a single joined trajectory, based on which PCA and clustering analysis were developed by using AmberTools16 (considering the Ca atoms). The first two

eigenvectors were considered the reaction coordinates to construct the two-dimensional FEL based on PCA as reported elsewhere [43]. From PCA, a correlation map was constructed to observe those groups of atoms that moved in a correlated manner. Figures were built by using PyMOL [44].

## 2.3.1 Binding free energy

The binding free energies of protein-ligand and protein-protein interactions were evaluated by using the MMGBSA approach [45] implemented in AmberTools16. MMGBSA is an end-point approach capable of obtaining the binding free energy ( $\Delta G_{\text{bind}}$ ) for protein-ligand and protein-protein complexes based purely on the ensemble of the bound complexes without contemplating either the physical or the non-physical intermediates [46]. The binding free energy was estimated over the last 0.4  $\mu\text{s}$  of equilibrated simulation time, saving 4000 representative conformations. The solvation free energy was determined by using implicit solvent models [47], ionic strength of 0.15 M, and solute and solvent dielectric constants of 4 and 80, respectively. The binding free energies were estimated as described elsewhere [48].

## 3. Results

### 3.1 Stability of the simulated RXR $\alpha$ -PPAR $\gamma$ -DNA and RXR $\alpha$ -PPAR $\gamma$ systems

The RMSD and Rg plots illustrate the mobility of the RXR $\alpha$ -PPAR $\gamma$ -DNA and RXR $\alpha$ -PPAR $\gamma$  systems when bound to RZG and 9CR. Triplicate simulations of the RXR $\alpha$ -PPAR $\gamma$ -DNA system showed that the RMSD (Fig. S1A) and Rg (Fig. S1C) for backbone atoms first achieve equilibrium at 0.1  $\mu\text{s}$  and then again at 0.6  $\mu\text{s}$ , with an average Rg of  $28.45 \pm 0.20$  Å. The RMSD (Fig. S1B) and Rg (Fig. S1D) for the RXR $\alpha$ -PPAR $\gamma$  system also achieve constant values between 0.1 and 0.6  $\mu\text{s}$ , with an average Rg of  $28.25 \pm 0.20$  Å. Therefore, we considered the last 0.4  $\mu\text{s}$  as the equilibrated part of each simulation.

### 3.2 Ligand interactions of the PPAR $\gamma$ -RXR $\alpha$ -DNA system

#### 3.2.1 RZG at the PPAR $\gamma$ binding pocket

Clustering analysis over the equilibrated simulation time allowed us to obtain the first, second, and third populated conformers, which provide information about the representative interactions during MD simulations. The first populated conformation of the RXR $\alpha$ -PPAR $\gamma$ -DNA system showed that RZG forms hydrogen bonds (HBs) through its TDZ headgroup with the sidechain and polar backbone atoms of E343. The TDZ headgroup also makes hydrophobic contacts with P227, M329, L333, S342, R288, and S289. The pyridyl tail is stabilized by F282, C285, Q286, I326, L330, I456, L469, and Y473 (Fig. 2A). The second populated conformer showed that the TDZ headgroup forms HBs with the sidechain and polar backbone atoms of E343, and with polar backbone atoms of C285 and S342. The TDZ headgroup also makes hydrophobic contacts with C285, M329, I326, L330, L333, and S289. The pyridyl group is stabilized by Q283, Q286, Y327, P359, F360, F363, M364, L452, L453, H449, and I456 (Fig. 2C). The third populated

complex also showed the HBs between the TDZ headgroup and the sidechain and polar backbone atoms of E343, and there is one HB between polar atoms of the pyridyl group and the side chain of S342. The TDZ headgroup also makes hydrophobic contacts with C285, S289, M329, L333, L340, and I341. The pyridyl group is bound by F282, Q283, Q286, I326, Y327, L330, F360, F363, and H449 (Fig. 2E). Comparison of the three conformers with the crystallographic structure (Fig. S2A) showed that the main differences are in the stabilization of the TDZ headgroup through HBs.

Based on MD simulations, HBs are mainly between the TDZ headgroup and E343 localized at  $\beta 2-\beta 4$ , whereas in the crystallographic structure, the TDZ headgroup makes HBs with the sidechains of S289 (H3), H323 (H4/5), and Y473 (H12). With respect to hydrophobic interactions, most of the interactions localized at H3 (F282, C285, Q286, and S289), H4/5 (Y327 and L330),  $\beta 2-\beta 4$  (I341), H6 (L353), H7 (M364), and H10/11 (H449), observed in the co-co-crystallized complex (Fig. S2A), are still present during simulations.

### 3.2.2 9CR at the RXR $\alpha$ binding pocket

In the first populated RXR $\alpha$ -PPAR $\gamma$ -DNA system, 9CR makes a series of van der Waals contacts with the ligand binding site of RXR $\alpha$ . The carboxylate of 9CR makes polar interactions with N262. The triene portion and the  $\beta$  ionone establish interactions with P264, T266, C269, A272, Q275, L276, T278, W305, L451, and M454 (Fig. 2B). In the second populated conformation, the carboxylate of 9CR forms one HB with backbone atoms of A327. The hydrophobic regions establish interactions with N262, P264, T266, C269, A272, Q275, L276, T278, L279, W305, L309, L451, and M454 (Fig. 2D). In the third conformation, the carboxylate of 9CR forms one HB with the side chain of S260. The nonpolar region establishes interactions with N262, P264, T266, C269, A272, Q275, L276, L279, W305, L309, and M454 (Fig. 2F). Comparison with the crystallographic structure (Fig. S2B) showed that during MD simulations, the carboxylate of 9CR changes into different conformations that allow the formation of HBs with only one residue (A327) of the two observed in the crystallographic structures, and with other residues (N262 and S260) not present in the crystallographic structure. With respect to hydrophobic interactions, MD simulations revealed that some interactions along H3 (A272 and Q275), H4/H5 (W305), and the loop between H4/H5 and H6 (A327) observed in the co-co-crystallized complex (Fig. S2B) are still present. In addition, in MD simulations there are some new hydrophobic interactions along H3 (P264, T266, C269, A272, Q275, L276, and T278), H4/H5 (W305 and L309), and AF-2 (L451 and M454) not present in the crystallographic complex.

## 3.3 Ligand interactions of the RXR $\alpha$ -PPAR $\gamma$ system

### 3.3.1 RZG at the PPAR $\gamma$ binding pocket

The first populated conformer of the RXR $\alpha$ -PPAR $\gamma$  system showed that RZG makes one HB involving the TDZ headgroup and the sidechain of Y473, a characteristic HB involved in stabilizing a full agonist in the active state of the RXR $\alpha$ -PPAR $\gamma$  system [20, 49]. The TDZ headgroup also forms contacts with F282, S289, H449, L452, and L469. The pyridyl tail is bound by I262, C285, I326, Y327, L330, and I341 (Fig. 3A).

These interactions are comparable to those observed in the crystallographic complex of the RXR $\alpha$ -PPAR $\gamma$ -DNA complex (Fig. 2A). The second populated complex showed that the HBs occur between the TDZ headgroup and the sidechains of Y327, H449, Y473, and Q286. The TDZ headgroup forms hydrophobic contacts with S289, H323, I326 and F363. The pyridyl tail is attached by C285, R288, L330, L340, I341, S342, and M364 (Fig. 3C). The third populated complex illustrated that the TDZ group establishes HBs with Q286, S289, and H323. The TDZ headgroup makes hydrophobic contacts with I326, Y327, F282, F363, and Y473. The pyridyl tail is attached by I262, G284, C285, I341, M348, and M364 (Fig. 3E). Comparison of the three conformers with the crystallographic structure revealed that despite the differences in how the TDZ headgroup is stabilized through HBs (Fig. S1), there are interactions between the TDZ headgroup and S289 (H3), H323 (H4/5), and Y473 (H7), in addition to other HBs with residues of H3 (Q286), H4/5 (Y327) and H10/11 (H449) not present in the crystallographic complex. These polar interactions are in line with those observed through MD simulations employing the monomeric state of PPAR $\gamma$  with different compounds containing the TDZ group [50]. With respect to hydrophobic interactions, most of the interactions localized at H3 (F282, C285, Q286, R288, and S289), H4/5 (Y327 and L330),  $\beta$ 2- $\beta$ 4 (341), H7 (M364), and H10/11 (H449) detected in the co-crystallized complex (Fig. S2A) are even present in MD simulations.

### 3.3.2 9CR at the RXR $\alpha$ binding pocket

In the first populated RXR $\alpha$ -PPAR $\gamma$  complex, 9CR is bound by a series of van der Waals interactions with V265, N267, F313 I324, V332 S336, A340, and V342 (Fig. 3B). In the second conformation, 9CR establishes nonpolar interactions with V265, T266, L326, V332, V342, C432, L436, I447, and F439 (Fig. 3D). In the third conformation, the ligand is bound by P264, V265, L326, V342, V349, I345, and C432. Comparison with the crystallographic structure showed that during MD simulations, the carboxylate of 9CR changes into different conformations that do not allow the formation of HBs (Fig. S2B).

MD simulations also showed that some hydrophobic interactions in H4/H5 (F313), the loop between H4/H5 and H6 (L326), H7 (V342 and I345), H10/11 (C432), and AF-2 (L436) observed in the co-crystallized complex (Fig. S2B) are still present. Taken together, the MD simulations revealed some new hydrophobic interactions in H3 (P264, V265, T266, and N267), the loop between H4/H5 and H6 (I324 and V332), H6 (S336 and A340), H7 (V349), H10/11 (F439), and AF-2 (I447) not present in the crystallographic complex. Comparison between the RXR $\alpha$ -PPAR $\gamma$ -DNA and RXR $\alpha$ -PPAR $\gamma$  systems during simulations showed that the latter share more interactions with the crystallographic complex than the PPAR $\gamma$ -RXR $\alpha$ -DNA system. This finding suggests that the ternary complex has a greater impact on 9CR binding to RXR $\alpha$  than RGZ binding to PPAR $\gamma$ .

## 3.4 The protein-protein interactions of the RXR $\alpha$ -PPAR $\gamma$ -DNA and RXR $\alpha$ -PPAR $\gamma$ systems

The heterodimeric interface of the RXR $\alpha$ -PPAR $\gamma$ -DNA and RXR $\alpha$ -PPAR $\gamma$  systems is stabilized by more protein-protein interactions than those present in the co-crystallized complex (Table S1). Some similar interactions present during simulations and the in the co-crystallized complex are those involving the

DBD, the hinge, H7, loop<sub>H8-H9</sub>, and H10/11 of RXR $\alpha$ , and the DBD,  $\beta 2-\beta 4$ , H6, H7, H9, and H10/11 of PPAR $\gamma$ . In the RXR $\alpha$ -PPAR $\gamma$  system, the protein-protein interface is mostly stabilized by residues of the DBD and the hinge of RXR $\alpha$ , forming interactions with residues of the DBD,  $\beta 2-\beta 4$ , H2, H6, H7, and H10/11 of PPAR $\gamma$ . For the RXR $\alpha$ -PPAR $\gamma$ -DNA system, the protein-protein interface is mostly structured by residues of H7, H9, loop<sub>H8-H9</sub>, and H10/11 of RXR $\alpha$ , forming interactions with residues of H7, H8, loop<sub>H8-H9</sub>, H9, and H10/11 of PPAR $\gamma$ . Comparison between the RXR $\alpha$ -PPAR $\gamma$ -DNA and RXR $\alpha$ -PPAR $\gamma$  systems revealed more interactions for the latter system, mostly through the DBD and the hinge of RXR $\alpha$  with residues of the LBD of PPAR $\gamma$ . In contrast, in the RXR $\alpha$ -PPAR $\gamma$ -DNA system, most of the interactions are through the LBD of both receptors. These structural differences suggest different protein-protein affinity that would also impact the affinity of each ligand to bind to RXR $\alpha$  and PPAR $\gamma$ .

### **3.5 Binding free energy calculations of protein-ligand interactions using MMGBSA**

Binding free energy ( $\Delta G_{\text{MMGBSA}}$ ) values determined with the MMGBSA approach for protein-ligand and protein-protein interactions are energetically favorable (Table 1). The changes in solvation free energy using GB ( $\Delta G_{\text{solv-GBSA}}$ ) revealed that RZG shows a higher desolvation cost of binding than 9CR. In fact, this term contributes favorably for 9CR binding, in contrast to RZG binding, and this is appreciated for the RXR $\alpha$ -PPAR $\gamma$ -DNA and RXR $\alpha$ -PPAR $\gamma$  systems. Table 1 also shows that the protein-ligand interaction energy ( $\Delta E_{\text{MM}}$ ) is energetically favorable for RZG binding in the RXR $\alpha$ -PPAR $\gamma$ -DNA and RXR $\alpha$ -PPAR $\gamma$  systems, and 9CR binding in the RXR $\alpha$ -PPAR $\gamma$ -DNA system, but not the RXR $\alpha$ -PPAR $\gamma$  system. Despite these differences, the  $\Delta G_{\text{MMGBSA}}$  values are thermodynamically favorable for RGZ and 9CR binding in the RXR $\alpha$ -PPAR $\gamma$ -DNA and RXR $\alpha$ -PPAR $\gamma$  systems. Interestingly, whereas the affinity of RGZ in both systems is similar, the affinity of 9CR in the RXR $\alpha$ -PPAR $\gamma$ -DNA system is higher than in the RXR $\alpha$ -PPAR $\gamma$  system, suggesting that DNA binding by part of the RXR $\alpha$ -PPAR $\gamma$  system has greater impact on molecular recognition at the RXR $\alpha$  ligand binding site.

Table 1

Binding free energy components for protein-ligand and protein-protein interactions of the RXR $\alpha$ -PPAR $\gamma$ , and RXR $\alpha$ -PPAR $\gamma$ -DNA systems are calculated by using MMGBSA approach (values are in Kcal/mol).

System	$\Delta E_{MM}$	$\Delta G_{solv-GBSA}$	$\Delta G_{MMGBSA}$
PPAR $\gamma$ -RXR $\alpha$			
PPAR $\gamma_{9RSG}$	-67.12 $\pm$ 3.0	26.26 $\pm$ 3.0	-40.86 $\pm$ 5.0
RXR $\alpha_{9CR}$	4.84 $\pm$ 1.0	-34.88 $\pm$ 4.0	-30.04 $\pm$ 3.0
PPAR $\gamma$ -RXR $\alpha$ -DNA			
PPAR $\gamma_{9RSG}$	-69.21 $\pm$ 3.0	26.43 $\pm$ 3.0	-42.78 $\pm$ 5.0
RXR $\alpha_{9CR}$	-165.84 $\pm$ 13.0	-205.27 $\pm$ 12.0	-39.43 $\pm$ 3.0
Protein-protein			
PPAR $\gamma$ -RXR $\alpha$	-1522.99 $\pm$ 138.0	1403.39 $\pm$ 132.0	-119.59 $\pm$ 18.0
PPAR $\gamma$ -RXR $\alpha$ -DNA	-993.43 $\pm$ 112.0	898.59 $\pm$ 106.0	-94.84 $\pm$ 13.0

## 3.6 Binding free energy calculations of protein-protein interactions using MMGBSA

Based on the changes in solvation free energy using GB, the RXR $\alpha$ -PPAR $\gamma$  system has a higher desolvation cost of protein-protein binding than the RXR $\alpha$ -PPAR $\gamma$ -DNA system, contributing unfavorably to the  $\Delta G_{MMGBSA}$  value (Table 1). The protein-protein interaction energy ( $\Delta E_{MM}$ ) is energetically more favorable for the RXR $\alpha$ -PPAR $\gamma$  system than the RXR $\alpha$ -PPAR $\gamma$ -DNA system, consistently with the finding that there are more interactions for the RXR $\alpha$ -PPAR $\gamma$  system than the RXR $\alpha$ -PPAR $\gamma$ -DNA system (Table S1). The affinity of the RXR $\alpha$ -PPAR $\gamma$  system is higher than the RXR $\alpha$ -PPAR $\gamma$ -DNA system, indicating that DNA binding by part of the RXR $\alpha$ -PPAR $\gamma$  system contributes to decrease the affinity between both receptors. Considering the differences in the protein-ligand and protein-protein affinity for the RXR $\alpha$ -PPAR $\gamma$  than RXR $\alpha$ -PPAR $\gamma$ -DNA systems, we can conclude that DNA binding by part of the RXR $\alpha$ -PPAR $\gamma$  system contributes to decrease the protein-protein affinity but increases the ligand affinity at the RXR $\alpha$  binding site.

## 3.7 Per-residue free energy decomposition

### 3.7.1 Per-residue free energy decomposition of the PPAR $\gamma_{RZG}$ complex

Table S2 shows the energies for each residue participating in the protein-ligand interactions of the RXR $\alpha$ -PPAR $\gamma$  and RXR $\alpha$ -PPAR $\gamma$ -DNA systems. In the RXR $\alpha$ -PPAR $\gamma$ -DNA system, the major

contributors to the binding affinity ( $\Delta G_{\text{MMGBSA}} \geq 1.0$  kcal) in the  $\text{PPAR}\gamma_{\text{RZG}}$  complex are F282, C285, Q286, I326, L330, I341, E343, and His449 (Table 2). Of these residues, E343 forms HBs through its polar backbone atoms and side chain with the TDZ headgroup (Fig. 2A, 2C and 2E), whereas the rest stabilize RGZ through hydrophobic interactions. For the  $\text{PPAR}\gamma_{\text{RZG}}$  complex in the  $\text{RXR}\alpha$ - $\text{PPAR}\gamma$ -DNA system, the major contributors to the affinity are C285, Q286, R288, I326, Y327, L330, I341, and H449. These residues mostly form hydrophobic interactions. Comparison of RGZ stabilization in both systems revealed that this ligand is better stabilized in the  $\text{RXR}\alpha$ - $\text{PPAR}\gamma$ -DNA system, with more residues contributing to the binding affinity.

Table 2  
Per-residue free energy for protein-ligand interactions of the  $\text{RXR}\alpha$ - $\text{PPAR}\gamma$ -DNA, and  $\text{RXR}\alpha$ - $\text{PPAR}\gamma$  systems coupled to RGZ and 9CR (values are in kcal/mol).

Residue	$\text{PPAR}\gamma$ - $\text{RXR}\alpha$ -DNA $\text{PPAR}\gamma_{\text{RSG}}$	$\text{PPAR}\gamma$ - $\text{RXR}\alpha$ $\text{PPAR}\gamma_{\text{RSG}}$	Residue	$\text{PPAR}\gamma$ - $\text{RXR}\alpha$ -DNA $\text{RXR}\alpha_{9\text{CR}}$	$\text{PPAR}\gamma$ - $\text{RXR}\alpha$ $\text{RXR}\alpha_{9\text{CR}}$
F282	-1.974		N262	-3.226	
C285	-1.181	-2.765	P264	-1.621	
Q286	-3.206	-1.313	N267		-1.006
R288		-1.726	ALA272	-1.322	
I326	-1.096	-1.191	Q275	-2.501	
Y327		-1.316	L276	-1.779	
L330	-2.373	-1.623	W305	-1.391	
I341	-1.303	-2.386	L309	-1.242	
E343	-1.035		L326		-1.503
H449	-1.179	-1.026	V332		-1.061
			V342		-1.775
			I345		-1.238
			L451	-1.695	

### 3.7.2 Per-residue free energy decomposition of the $\text{RXR}\alpha_{9\text{CR}}$ complex

In the  $\text{RXR}\alpha$ - $\text{PPAR}\gamma$ -DNA system, the main sources of the binding free energy for  $\text{RXR}\alpha_{9\text{CR}}$  are N262, P264, A272, Q275, L276, W305, L309, and L451 (Table 2). Each of these residues participates in hydrophobic interactions, except for N262, which forms HBs (Fig. 2B and 2D). For  $\text{RXR}\alpha_{9\text{CR}}$  in the  $\text{RXR}\alpha$ - $\text{PPAR}\gamma$  system, the major contributors to the affinity are N267, L326, V332, V342, and I345, which form

hydrophobic interactions. Comparison of the interactions that mainly contribute to the binding free energy in RXR $\alpha$ <sub>9CR</sub> indicated that 9CR is stabilized better in the RXR $\alpha$ -PPAR $\gamma$ -DNA system. Furthermore, the residues participating in ligand stabilization are different in the two systems, indicating that DNA binding to the RXR $\alpha$ -PPAR $\gamma$  system increases the stability of 9CR binding to RXR $\alpha$ .

### 3.7.3 Per-residue free energy decomposition of the RXR $\alpha$ -PPAR $\gamma$ system

Table S3 lists the energies for each protein-protein interaction that maintains the RXR $\alpha$ -PPAR $\gamma$  and RXR $\alpha$ -PPAR $\gamma$ -DNA systems. In the RXR $\alpha$ -PPAR $\gamma$  system, the main sources of the binding free energy in the heterodimeric complex are Y169, R184, Y192, R209, N216, E219, E394, Y397, and R421 for RXR $\alpha$  (Table 3). Of these residues, Y169, R184, Y192, N216, and E219 are localized along the DBD, whereas E394 and R421 belong to H9 and H10/11, respectively. Regarding PPAR $\gamma$ , R153, D337, E351, E378, E396, Q430, K434, and Q437 are the main contributors to the complex affinity.

Table 3

Per-residue free energy for protein-protein interactions of the RXR $\alpha$ -PPAR $\gamma$ -DNA, and RXR $\alpha$ -PPAR $\gamma$  systems coupled to RZG and 9CR (values are in Kcal/mol). Residues at the left and right correspond to RXR $\alpha$  and PPAR $\gamma$ , respectively.

RXR $\alpha$ -PPAR $\gamma$	Energy	RXR $\alpha$ -PPAR $\gamma$ -DNA	Energy
(DBD) Y169.OH-E351.OE2 (H6)	-6.30	(DBD) L196.CD1-F347.CE1 ( $\beta$ 2- $\beta$ 4)	-3.50
(DBD) R184.NH2-E351.OE2 (H6)	-5.90	(DBD) R202.NE-D337.OD2 ( $\beta$ 2- $\beta$ 4)	-5.80
(DBD) Y192.OH-D337.OD1 ( $\beta$ 2- $\beta$ 4)	-8.50	(DBD) E214.OD2-R153.NE (DBD)	-4.80
(DBD) R209.NE-E378.OE2 (H7)	-3.60	(H9) E394.OE1-K434.NZ (H10/11)	-3.90
		(H9) E394.OE1-S429.OG (H10/11)	
(DBD) N216.OD1-Q430.NE2 (H10/11)	-4.40	(H10/11) L419.CB-L436.CD1 (H10/11)	-4.50
(DBD) E219.OE1-R153.NH1 (DBD)	-3.90	(H10/11) L420.CD2-L414.CD1 (H9)	-4.80
		(H10/11) L420.CD1-M439.CE	
		(H10/11)	
(H9) E394.O-Q430.NE2 (H10/11)	-6.50	(H10/11) R421.NH1-D396.OD2	-7.30
(H9) E394.OE1-K434.NZ (H10/11)		(L <sub>H8-H9</sub> )	
(H9) Y397.OH-Q437.OE1 (H10/11)	-4.90	(H10/11) S427.OG-T447.OG1	-5.70
		(H10/11)	
(H10/11) R421.NH1-D396.OD1	-5.50	(H10/11) K431.NZ-Q451.OE1	-6.00
(L <sub>H8-H9</sub> )		(H10/11)	
		(H10/11) K431.NZ-Y477.OXT (AF-2)	
Residues at the left and right correspond to RXR $\alpha$ and PPAR $\gamma$ , respectively.			

These residues are localized in the DBD (R153),  $\beta 2$ – $\beta 4$  (D337), H6 (E351), H7 (E378), loop<sub>H8–H9</sub> (E396), and H10/11 (Q430, K434 and Q437) (Table 3).

In the RXR $\alpha$ –PPAR $\gamma$ –DNA system, the contributing residues are L196, R202, D214, E394, L419, L420, R421, S427, and K431 for RXR $\alpha$ . These residues are located in the DBD (L196 and R202), the hinge (D214), H9 (E394), and H10/11 (L419, L420, R421, S427, and K431) (Table 3). With respect to PPAR $\gamma$ , D337, D396, L414, S429, K434, L436, M439, T447, Q451, and Y477 are the main residues that affect the affinity. These residues are located in  $\beta 2$ – $\beta 4$  (D337), loop<sub>H8–H9</sub> (D396), H9 (L414), H10/11 (S429, K434, L436, M439, T447, and Q451) and H12 (Y477) (Table 3).

Although both systems share several protein–protein interactions (Table S3), those that contribute to  $\Delta G_{\text{MMGBSA}}$  are dissimilar (Table 3), indicating that DNA binding by the RXR $\alpha$ –PPAR $\gamma$  system impacts the affinity as well as the type of interactions responsible for binding. Considering the protein regions that mostly contribute to  $\Delta G_{\text{MMGBSA}}$ , the structural domains that guide protein–protein recognition in the RXR $\alpha$ –PPAR $\gamma$  system are the DBD, H9, and H10/11 of RXR $\alpha$ , and the DBD,  $\beta 2$ – $\beta 4$ , H6, H7, loop<sub>H8–H9</sub>, and H10/11 of PPAR $\gamma$ . For the RXR $\alpha$ –PPAR $\gamma$ –DNA system, the domains are the DBD, the hinge, H9, and H10/11 of RXR $\alpha$ , and  $\beta 2$ – $\beta 4$ , loop<sub>H8–H9</sub>, H9, H10/11, and H12 of PPAR $\gamma$ . These differences suggest that PPAR $\gamma$  has a greater role in regulation of the free and bound DNA state, a finding in line with previous MD simulations using the RXR $\alpha$ –PPAR $\gamma$ –DNA system [33].

## 3.8 PCA

PCA was carried out to extract the most important eigenvectors. For the RXR $\alpha$ –PPAR $\gamma$  and RXR $\alpha$ –PPAR $\gamma$ –DNA systems, the first two eigenvectors (PC1 and PC2) contain the largest eigenvalues, contributing 48.0% and 43.0%, respectively, to the total fluctuation of the two systems. PC1 versus PC2 contains the main conformational states sampled by simulations for the RXR $\alpha$ –PPAR $\gamma$  (Fig. 4A) and RXR $\alpha$ –PPAR $\gamma$ –DNA (Fig. 4B) systems. This comparison provided information about the conformational complexity by reconstructing the FEL (Fig. 4C and 4D). Projection of the motion in the phase space along the first and second eigenvectors (PC2 versus PC1) for the RXR $\alpha$ –PPAR $\gamma$  system (Fig. 4C) covers a larger region in the essential subspace than that of the RXR $\alpha$ –PPAR $\gamma$ –DNA system (Fig. 4D), suggesting a larger conformational entropy for the RXR $\alpha$ –PPAR $\gamma$  system. Figure 4C and 4D show the two-dimensional FEL of the two-member system utilizing the first two eigenvector projections as the reaction coordinates. The FEL indicates that although the RXR $\alpha$ –PPAR $\gamma$ –DNA system shows greater occupancy of the major stable conformational ensembles, two of the major conformational ensembles for the RXR $\alpha$ –PPAR $\gamma$  system (Fig. 4C) are larger than those in the RXR $\alpha$ –PPAR $\gamma$ –DNA system. These findings indicate that the RXR $\alpha$ –PPAR $\gamma$  system samples more of the most thermostable conformations during the simulations.

## 3.9 Dynamic correlated motions

We performed dynamic correlation analysis to explore the intradomain correlations within the PPAR $\gamma$  and RXR $\alpha$  and in the heterodimer state (Fig. S3). The correlated motions among different regions of RXR $\alpha$  in

the RXR $\alpha$ -PPAR $\gamma$ -DNA system are through hinge-H1, H1-H2, H2-H3, H3-H4/5, H4/5-H7, H7-H9, and H10/11-H12 (Table 4). Of the residues participating in these correlated motions, C269 localized in H3 interacts directly with 9CR (Fig. 2B, 2D, and 2F), and E219 in the hinge participates in protein-protein interactions with Q163 at the DBD of PPAR $\gamma$  (Table S3).

For PPAR $\gamma$  in the RXR $\alpha$ -PPAR $\gamma$ -DNA system, the correlated motions are through DBD-hinge, hinge-H1, H1-H2, H2-H3, H3-H4/5, H4/5-H7, H7-H9, and H10/11-H12 (Table 4). From the residues participating in these correlated motions, F363 and M364 localized in H7 interact directly with RZG (Fig. 2C and 2E). R357 is in close contact with these residues; it has been reported to be important to regulate ligand dissociation [51]. Therefore, correlated motions involving R357 can be a mechanism of regulating ligand dissociation. H449 in H10/11 participates in protein-ligand interactions with RZG (Table S3). This residue is in close proximity to residues forming protein-protein interactions with H10/11 of RXR $\alpha$ , suggesting that correlated motions involving this residue might be a mechanism to regulate the protein-protein interface. Other residues (N312 and D313) in H4/5 whose correlations appeared in the RXR $\alpha$ -PPAR $\gamma$ -DNA system (Table S3) and are in close proximity to the coactivator binding site. Therefore, this correlation could be linked to modulation of a coactivator. In addition, there is one interdomain correlated motion between R136 in the DBD of PPAR $\gamma$  and H449 in H12 of RXR $\alpha$ , indicating correlated motions between the DBD of PPAR $\gamma$  and the active site of RXR $\alpha$ .

In the RXR $\alpha$ -PPAR $\gamma$  system, the correlated motions of RXR $\alpha$  are present through DBD-hinge, hinge-H1, H1-H2, H2-H4/5, H4/5-H7, H7-H9 and H10/11-H12 (Table 4). Among these correlated motions, L436 in H10/11 interacts directly with 9CR (Fig. 3D). E219 in the hinge and K356 at H7 form protein-protein interactions with R153 in the DBD and E407 in H9 of PPAR $\gamma$ , respectively (Table S3).

Table 4

Intradomain correlated motions of energy for the RXR $\alpha$ -PPAR $\gamma$ -DNA, and RXR $\alpha$ -PPAR $\gamma$  systems.

<b>System</b>	<b>Residues of RXR<math>\alpha</math></b>	<b>Residues of PPAR<math>\gamma</math></b>
RXR $\alpha$ -PPAR $\gamma$ -DNA	(DBD) K132:G199 (DBD)	(hinge)A188:L211(H1)
	(DBD) M200:E203 (DBD)	(H1)R212:A213(H1)
	(hinge) R209:D214 (hinge)	(H1)A215:K230(H2),
	(hinge) E219:L236 (H1)	(DBD)R140:Q187(hinge)
	(H2) 250, (H2)252:253(H2)	(DBD)R137:I139(DBD)
	(H3) C269:I299(H4/5)	(H9)E418:H449(H10/11)
	(H7)K356:E410(H9)	(H3)S274:D310(H4/5)
	(H1)E237:Y249(H2)	(H4/5)N312, (H7)M364:L417(H9),
	(H2)E251, (H2)M254:I268(H3)	(H10/11)V450:D462(H12),
	(H4/5)L300:S355 (H7)	(H1)L214, (H2)A231:Q273(H3),
	(H10/11)L418:D448(H12)	(H4/5)D313:F363(H7)
	RXR $\alpha$ -PPAR $\gamma$	Residues of RXR $\alpha$
(DBD)K132:G199(DBD)		(hinge)K190:E191(hinge),
(DBD)M200:E207(hinge)		(H9)Q415, (H10/11-H12)M463:E471(H12)
(DBD)E208:N218(hinge)		(hinge)A188:E189(hinge),
(hinge)E219:E239(H1)		(hinge)K192:L211(H1),
(H2)P258, (H2)S260:A303(H4/5)		(H3)E276:N312(H4/5),
(H7)K356:E410(H9),		(H7)D362:L414(H9),
(H10/11)429, (H10/11)F437:D448(H12),		(H9)A415:L416(H9),
(H1)L240:E251(H2)		(H1)R212: F247( $\beta$ 1),
(H2)A252:N257(H2)		(H2') E259:K275(H3),
(H2)S259, (H4/5)G304:S355(H7)		
(H9)Q411:I428(H9-H10/11),		(H4/5)D313:G361(H7)
(H10/11)L430:L436(H10/11)	( $\beta$ 1)V248:G258 (H2')	
	(H9)E418:V446(H10/11)	

<i>System</i>	<i>Residues of RXR<math>\alpha</math></i>	<i>Residues of PPAR<math>\gamma</math></i>
		H10/11)H449:D462(H12)

PPAR $\gamma$  in the RXR $\alpha$ –PPAR $\gamma$  system shows that the correlated motions take place through residues in hinge–H1, H1– $\beta$ 1,  $\beta$ 1–H2', H2'–H3, H3–H4/5, H4/5–H7, H7–H9, H9–H10/11, and H10/11–H12 (Table 4). Of these correlated motions, only G361 and D362 in H7 are close to two residues (F363 and M364) that interact directly with RZG (Fig. 3C and 3E). Only two residues (Q444 and T447) in H10/11 of PPAR $\gamma$  form protein–protein interactions with two residues (R426 and S427) in H10/11 of RXR $\alpha$  (Table S3). In the interdomain of the RXR $\alpha$ –PPAR $\gamma$  system, there is only one interaction between T449 in H12 of RXR $\alpha$  and Q187 in the hinge of PPAR $\gamma$ .

## 4. Discussion

Experimental data collected with X-ray crystallography, electron microscopy, and SAXS have provided structural insight regarding the active and inactive states of the RXR $\alpha$ –PPAR $\gamma$  system. In the active state, the RXR $\alpha$ –PPAR system is coupled to activating ligands and coactivators, which facilitate DNA binding, activating gene expression [25–27]. Previous MD simulations at the nanosecond timescale using the activated state of the RXR $\alpha$ –PPAR $\gamma$  system with DNA bound revealed a flux of correlated motions coming from DNA to the LBDs, with important participation of PPAR $\gamma$ –DBD compared with RXR $\alpha$  [33], results in agreement with hydrogen/deuterium exchange experiments of the permissive VDR–RXR complex [28]. In this study, we explored the structural and energetic basis of the molecular recognition between the active RXR $\alpha$ –PPAR system and DNA at the microsecond timescale. We employed the structure of RXR $\alpha$ –PPAR co-crystallized with their agonists and coactivators and forming or not forming a complex with DNA through its DBD (PDB entry 3DZY).

Clustering studies over the equilibrated simulation time revealed that the main regions contributing to the protein–ligand complex are similar for PPAR $\gamma$ <sub>RZG</sub> in the RXR $\alpha$ –PPAR $\gamma$  and RXR $\alpha$ –PPAR $\gamma$ –DNA systems; the only notable differences relate to stabilization of the TDZ headgroup. In contrast, RXR $\alpha$ <sub>9CR</sub> in the RXR $\alpha$ –PPAR $\gamma$  system is stabilized by more interactions in the LBD compared with the RXR $\alpha$ –PPAR $\gamma$ –DNA system, including H6, H7, and H10/11 by part of the RXR $\alpha$ –PPAR $\gamma$  system. Protein–protein interactions revealed more interactions for the RXR $\alpha$ –PPAR $\gamma$  system than the PPAR $\gamma$ –DNA system, mostly through the DBD and the hinge of RXR $\alpha$  with residues of the LBD of PPAR $\gamma$ . In contrast, in the RXR $\alpha$ –PPAR $\gamma$ –DNA system, most of the interactions are through the LBD of both receptors. Binding free energy calculations of protein–ligand interactions using the MMGBSA approach revealed that the affinity of RZG in PPAR $\gamma$ <sub>RZG</sub> complex is similar in both systems. In contrast, the affinity of 9CR in RXR $\alpha$ <sub>9CR</sub> is higher in the RXR $\alpha$ –PPAR $\gamma$ –DNA system. These differences suggest RXR $\alpha$ <sub>9CR</sub> plays an important role in modulating molecular recognition in the system. Binding free energy calculations of protein–protein interactions using the MMGBSA approach showed that coupling DNA to the RXR $\alpha$ –PPAR $\gamma$  heterodimer contributes to decrease the affinity between both partners, a finding consistent with the different protein–protein interactions observed in the two systems (Table S2).

Based on per-residue free energy decomposition analysis of the two systems, RZG is better stabilized in the RXR $\alpha$ -PPAR $\gamma$ -DNA system via more residues that contribute to the affinity. Similar analysis for 9CR showed that this ligand is better stabilized in the RXR $\alpha$ -PPAR $\gamma$ -DNA system, and the residues participating in stabilization are different in the two systems, indicating that DNA binding by the RXR $\alpha$ -PPAR $\gamma$  system significantly impacts molecular recognition of RZG and 9CR at the PPAR $\gamma$  and RXR $\alpha$  binding sites, respectively, but more importantly for the latter system. Per-residue free energy decomposition for the protein-protein interface revealed greater participation of RXR $\alpha$  residues (in the DBD, H9, and H10/11) than PPAR $\gamma$  residues (in the DBD,  $\beta$ 2- $\beta$ 4, H6, H7, loop<sub>H8-H9</sub>, and H10/11) in the RXR $\alpha$ -PPAR $\gamma$  system. For the RXR $\alpha$ -PPAR $\gamma$ -DNA system, the RXR $\alpha$  residues involved are also more important in recognition and are located in similar regions to those in the RXR $\alpha$ -PPAR $\gamma$  system. By contrast, the PPAR $\gamma$  residues involved are different than for the RXR $\alpha$ -PPAR $\gamma$  system, located in  $\beta$ 2- $\beta$ 4, loop<sub>H8-H9</sub>, H9, H10/11, and H12. Overall, PPAR $\gamma$  is more important in regulation of the system regardless of whether DNA is bound.

PCA and the FEL indicated that the RXR $\alpha$ -PPAR $\gamma$  system explores a larger conformational space and more major stable conformations than the RXR $\alpha$ -PPAR $\gamma$ -DNA system. Hence, DNA binding by the RXR $\alpha$ -PPAR $\gamma$  complex reduces the conformational entropy and decreases the number of major stable conformational ensembles, but thermostable conformations persist.

Correlated motions of RXR $\alpha$  in the RXR $\alpha$ -PPAR $\gamma$ -DNA system showed greater participation of structural elements in the LBD compared with the RXR $\alpha$ -PPAR $\gamma$  system. Both systems have correlated motions between the hinge and LBD for RXR $\alpha$ , but the motion between DBD-hinge-LBD only occurs in the RXR $\alpha$ -PPAR $\gamma$  system. These differences also impact protein-ligand interactions involving H3 and H10/11, and protein-protein interactions involving the hinge and H7.

Correlated motions of PPAR $\gamma$  in the RXR $\alpha$ -PPAR $\gamma$  system showed greater participation of structural elements in the LBD compared with the RXR $\alpha$ -PPAR $\gamma$ -DNA system. In both systems, there are correlated motions between the hinge and the LBD of RXR $\alpha$ ; however, the motion between DBD-hinge-LBD only occur for the RXR $\alpha$ -PPAR $\gamma$ -DNA system. Interestingly, these variations do not impact important protein-ligand interactions involving H7 and protein-protein interactions involving H10/11. The differences also impact the interdomain correlations for both systems, specifically between H12 of RXR $\alpha$  and the DBD of PPAR $\gamma$  for the RXR $\alpha$ -PPAR $\gamma$ -DNA system and between H12 of RXR $\alpha$  and the hinge of PPAR $\gamma$  for the RXR $\alpha$ -PPAR $\gamma$  system.

## 5. Conclusions

We used structural data and MD simulations coupled with the MMGBSA approach, PCA, the FEL, and correlated motion analyses to explore the structural and energetic differences between the RXR $\alpha$ -PPAR $\gamma$  and RXR $\alpha$ -PPAR $\gamma$ -DNA systems. Clustering and energetic analysis using the MMGBSA approach indicated that 9CR experiences more significant changes in affinity and map of interactions, whereas RZG shows some small differences. The affinity of the RXR $\alpha$ -PPAR $\gamma$  system is reduced upon DNA

binding. PCA and FEL studies revealed that DNA binding by the RXR $\alpha$ –PPAR $\gamma$  system reduces the conformational entropy, but thermostable conformations persist in both systems. There are correlated motions between the hinge and the LBD for RXR $\alpha$  or PPAR $\gamma$  forming part of the RXR $\alpha$ –PPAR $\gamma$  and RXR $\alpha$ –PPAR $\gamma$ –DNA systems, but the motion between DBD–hinge–LBD for RXR $\alpha$  or PPAR $\gamma$  only occurs for the RXR $\alpha$ –PPAR $\gamma$  system and the RXR $\alpha$ –PPAR $\gamma$ –DNA system, respectively, indicating that DBD–hinge–LBD correlated motions are more prominent for PPAR $\gamma$  than for RXR $\alpha$  when RXR $\alpha$ –PPAR $\gamma$  is bound to DNA. Taken together, we conclude that DNA binding by the RXR $\alpha$ –PPAR $\gamma$  system contributes to decrease the protein–protein affinity but increase the affinity of ligand at the RXR $\alpha$  binding site. Correlated motions suggest that the allosteric communication is also DNA dependent and bidirectional, impacting mainly the RXR $\alpha$  ligand. Based on this insight, we theorize that when designing new PPAR $\gamma$  agonists, it may be favorable to evaluate the structural and energetic changes and compare them with known PPAR $\gamma$  agonists.

## Declarations

**Conflicts of interest/Competing interests:** The authors declare they have no conflict of interest in terms of the content of this manuscript.

**Availability of data and material:** The datasets supporting the conclusions of this research are contained within the paper and its additional files.

**Code availability:** Not applicable.

**Authors' contributions:** Not applicable.

## References

1. Nagy L, Schwabe JW. Mechanism of the nuclear receptor molecular switch. *Trends Biochem Sci* 2004;29:317–324. [PubMed: 15276186]
2. Sonoda J, Pei L, Evans RM. Nuclear receptors: decoding metabolic disease. *FEBS Lett* 2008;582:2–9. [PubMed: 18023286]
3. Raghuram S, et al. Identification of heme as the ligand for the orphan nuclear receptors REV-ERB $\alpha$  and REV-ERB $\beta$ . *Nature Struct Mol Biol* 2007;14:1207–1213. [PubMed: 18037887]
4. Yin L, et al. Rev-erba, a heme sensor that coordinates metabolic and circadian pathways. *Science* 2007;318:1786–1789. [PubMed: 18006707]
5. Kersten, S., Desvergne, B. and Wahli, W. (2000) *Nature* 405, 421–424
6. B. Desvergne, W. Wahli, Peroxisome proliferator-activated receptors: nuclear control of metabolism, *Endocr. Rev.* 20 (5) (1999) 649–688.
7. P. Escher, W. Wahli, Peroxisome proliferator-activated receptors: insight into multiple cellular functions, *Mutat. Res.* 448 (2) (2000) 121–138.

8. J. Berger, D.E. Moller, The mechanisms of action of PPARs, *Annu. Rev. Med.* 53 (2002) 409–435,
9. G.M. Giordano Attianese, B. Desvergne, Integrative and systemic approaches for evaluating PPARbeta/delta (PPARD) function, *Nucl. Recept. Signal.* 13 (2015) e001,
10. Tontonoz, P., Hu, E. and Spiegelman, B.M. (1994) *Cell* 79, 1147–1156.
11. Lehrke, M. & Lazar, M. A. The many faces of ppar gamma. *Cell* 123, 993–999 (2005).
12. Ahmadian, M. et al. Ppar gamma signaling and metabolism: The good, the bad and the future. *Nat. Med.* 19, 557–566 (2013).
13. Lehman, J.M., Moore, L.B., Smith-Oliver, T.A., Wilkison, W.O., Willson, T.M. and Kliewer, S.A. (1995) *J. Biol. Chem.* 270, 12953–12956.
14. Willson, T.M., Cobb, J.E., Cowan, D.J., Wiethe, R.W., Correa, I.D., Prakash, S.R., Beck, K.D., Moore, L.B., Kliewer, S.A. and Lehnmann, J.M. (1996) *J. Med. Chem.* 39, 665–668.
15. Chawla A, Repa JJ, Evans RM, Mangelsdorf DJ. Nuclear receptors and lipid physiology: opening the X-files. *Science* 2001;294:1866–1870. [PubMed: 11729302]
16. Kliewer, S. A., Forman, B. M., Blumberg, B., Ong, E. S., Borgmeyer, U., Mangelsdorf, D. J., Umesono, K., & Evans, R. M. (1994). Differential Expression and Activation of a Family of Murine Peroxisome Proliferator-Activated Receptors. *Proceedings of the National Academy of Sciences of the United States of America*, 91(15), 7355–7359
17. Mangelsdorf DJ, Evans RM. The RXR heterodimers and orphan receptors. *Cell*. 1995 Dec 15;83(6):841–50.
18. McKenna, N. J., Lanz, R. B. & O'Malley, B. W. Nuclear receptor coregulators: Cellular and molecular biology. *Endocr. Rev.* 20, 321–344 (1999).
19. Gronemeyer, H., Gustafsson, J. A. & Laudet, V. Principles for modulation of the nuclear receptor superfamily. *Nat. Rev. Drug Discovery* 3, 950–964 (2004).
20. Nolte, R. T. et al. Ligand binding and co-activator assembly of the peroxisome proliferator-activated receptor-gamma. *Nature* 395, 137–143 (1998).
21. V. Zoete, A. Grosdidier, O. Michielin, Peroxisome proliferator-activated receptor structures: ligand specificity, molecular switch and interactions with regulators, *Biochim. Biophys. Acta* 1771 (8) (2007) 915–925,
22. R.T. Gampe Jr., V.G. Montana, M.H. Lambert, A.B. Miller, R.K. Bledsoe, M.V. Milburn, et al., Asymmetry in the PPARgamma/RXRalpha crystal structure reveals the molecular basis of heterodimerization among nuclear receptors, *Mol. Cell* 5 (3) (2000) 545–555
23. J.N. Feige, L. Gelman, L. Michalik, B. Desvergne, W. Wahli, From molecular action to physiological outputs: peroxisome proliferator-activated receptors are nuclear receptors at the crossroads of key cellular functions, *Prog. Lipid Res.* 45 (2) (2006) 120–159,
24. Hughes TS, Giri PK, de Vera IM, Marciano DP, Kuruvilla DS, Shin Y, Blayo AL, Kamenecka TM, Burris TP, Griffin PR, Kojetin DJ. An alternate binding site for PPARγ ligands. *Nat Commun.* 2014 Apr 7;5:3571. doi: 10.1038/ncomms4571. PMID: 24705063; PMCID: PMC4070320.

25. G.A. Francis, E. Fayard, F. Picard, J. Auwerx, Nuclear receptors and the control of metabolism, *Annu. Rev. Physiol.* 65 (2003) 261–311, <http://dx.doi.org/10.1146/annurev.physiol.65.092101.142528> (Epub 2003/01/09. PubMed PMID: 12518001).
26. P. Tontonoz, B.M. Spiegelman, Fat and beyond: the diverse biology of PPAR $\gamma$ , *Annu. Rev. Biochem.* 77 (2008) 289–312,
27. S.H. Rho, H.H. Park, G.B. Kang, Y.J. Im, M.S. Kang, B.K. Lim, et al., Crystal structure of *Bacillus subtilis* CodW, a noncanonical HslV-like peptidase with an impaired catalytic apparatus, *Proteins* 71 (2) (2008) 1020–1026
28. Zhang, J. et al. DNA binding alters coactivator interaction surfaces of the intact vdr-rxr complex. *Nat. Struct. Mol. Biol.* 18, 556–U172 (2011).
29. Hall, J. M., McDonnell, D. P. & Korach, K. S. Allosteric regulation of estrogen receptor structure, function, and coactivator recruitment by different estrogen response elements. *Mol. Endocrinol.* 16, 469–486 (2002).
30. Meijsing, S. H. et al. DNA binding site sequence directs glucocorticoid receptor structure and activity. *Science* 324, 407–410 (2009)
31. T. Venalainen, F. Molnar, C. Oostenbrink, C. Carlberg, M. Perakyla, Molecular mechanism of allosteric communication in the human PPAR $\alpha$ -RXR $\alpha$  heterodimer, *Proteins* 78 (4) (2010) 873–887, <http://dx.doi.org/10.1002/prot.22613> (PubMed PMID: 19847917).
32. Amber-Vitos O, Chaturvedi N, Nachliel E, Gutman M, Tsfadia Y. The effect of regulating molecules on the structure of the PPAR-RXR complex. *Biochim Biophys Acta.* 2016;1861(11):1852–1863. doi:10.1016/j.bbali.2016.09.003
33. Ricci, Clarisse G., et al. "Allosteric Pathways in the PPAR $\gamma$ -RXR $\alpha$  nuclear receptor complex." *Scientific Reports* 6 (2016): 19940.
34. Kurokawa, R. et al. Regulation of retinoid signaling by receptor polarity and allosteric control of ligand-binding. *Nature* 371, 528–531 (1994)
35. B. Webb, A. Sali. Comparative Protein Structure Modeling Using Modeller. *Current Protocols in Bioinformatics* 54, John Wiley & Sons, Inc., 5.6.1–5.6.37, 2016.
36. Chen VB, Arendall WB 3rd, Headd JJ, Keedy DA, Immormino RM, Kapral GJ, Murray LW, Richardson JS, Richardson DC. MolProbity: all-atom structure validation for macromolecular crystallography. *Acta Crystallogr D Biol Crystallogr.* 2010 Jan;66(Pt 1):12–21.
37. Price, D.J.; Brooks III, C.L. A modified TIP3P water potential for simulation with Ewald summation. *J. Chem. Phys.* 2004, 121, 10096–10103, doi:10.1063/1.1808117.
38. Duan, Y., Wu, C., Chowdhury, S., Lee, M.C., Xiong, G., Zhang, W., Yang, R., Cieplak, P., Luo, R., Lee, T., Caldwell, J., Wang, J., Kollman, P., 2003. A Point-Charge Force Field for Molecular Mechanics Simulations of Proteins Based on Condensed-Phase Quantum Mechanical Calculations. *J. Comput. Chem.* 24, 1999–2012.
39. Galindo-Murillo R, et al. Assessing the current state of amber force field modifications for DNA. *J. Chem. Theory Comput.* 2016;12:4114–4127.

40. Wang, J., Wolf, R.M., Caldwell, J.W., Kollman, P.A., Case, D.A., 2004. Development and testing of a general Amber force field. *J. Comput. Chem.* 25, 1157–1174.
41. Van Gunsteren, W.F., Berendsen, H.J.C., 1977. Algorithms for macromolecular dynamics and constraint dynamics. *Mol. Phys.* 34, 1311–1327.
42. Darden, T., York, D., Pedersen, L., 1993. Particle mesh Ewald: An N·log(N) method for Ewald sums in large systems. *J. Chem. Phys.* 98, 10089–10092.
43. Zhang, Z. B., Xia, Y. L., Shen, J. X., Du, W. W., Fu, Y. X., & Liu, S. Q. (2022). Mechanistic origin of different binding affinities of SARS-CoV and SARS-CoV-2 spike RBDs to human ACE2. *bioRxiv*.
44. DeLano, W. L. (2002). The PyMOL molecular graphics system. Palo Alto, CA: DeLano Scientific.
45. Belouzard, S., Millet, J.K., Licitra, B.N., Whittaker, G.R., 2012. Mechanisms of coronavirus cell entry mediated by the viral spike protein. *Viruses* 4, 1011–1033.
46. Du, X.; Li, Y.; Xia, Y.L.; Ai, S.M.; Liang, J.; Sang, P.; Ji, X.L.; Liu, S.Q. Insights into Protein-Ligand Interactions: Mechanisms, 917 Models, and Methods. *Int. J. Mol. Sci.* 2016, 17, doi:10.3390/ijms17020144.
47. Feig, M., Onufriev, A., Lee, M.S., Im, W., Case, D.A., Brooks, C.L., 2004. Performance Comparison of Generalized Born and Poisson Methods in the Calculation of Electrostatic Solvation Energies for Protein Structures. *J. Comput. Chem.* 25, 265–284.
48. Bello, M., 2018. Binding mechanism of kinase inhibitors to EGFR and T790M, L858R and L858R/T790M mutants through structural and energetic analysis. *Int. J. Biol. Macromol.* 118, 1948–1962.
49. Xu, H. E. et al. Molecular recognition of fatty acids by peroxisome proliferator-activated receptors. *Mol. Cell* 3, 397–403 (1999).
50. Álvarez-Almazán S, Bello M, Tamay-Cach F, Martínez-Archundia M, Alemán-González-Duhart D, Correa-Basurto J, Mendieta-Wejebe JE. Study of new interactions of glitazone's stereoisomers and the endogenous ligand 15d-PGJ2 on six different PPAR gamma proteins. *Biochem Pharmacol.* 2017 Oct 15;142:168–193.
51. Genest, D. et al. Ligand-escape pathways from the ligand-binding domain of ppar gamma receptor as probed by molecular dynamics simulations. *Eur. Biophys. J.* 37, 369–379 (2008).

## Supplementary Information

Figures S1-S3 and Tables S1-S3 are not available with this version.

## Figures

### Figure 1

Structural topology of the RXR $\alpha$ –PPAR $\gamma$ –DNA system. PPAR $\gamma$  and RXR $\alpha$  are presented in green and purple, respectively. For each receptor, a flexible hinge connects the DBD and the LBD.

## Figure 2

Protein-ligand interactions of RGZ and 9CR in the PPAR $\gamma$ –RXR $\alpha$ –DNA system. Interactions with RGZ and 9CR at the ligand-binding site of PPAR $\gamma$  and RXR $\alpha$ , respectively, are present in the first [RGZ (A) and 9CR (B)], second [RGZ (C) and 9CR (D)], and third [RGZ (E) and 9CR (F)] most populated conformations. Dot lines indicate HBs.

## Figure 3

Map of interactions of RGZ and 9CR in the PPAR $\gamma$ –RXR $\alpha$  system. Interactions of RGZ and 9CR at the ligand-binding site of PPAR $\gamma$  and RXR $\alpha$ , respectively, are present in the first [RGZ (A) and 9CR (B)], second [RGZ (C) and 9CR (D)], and third [RGZ (E) and 9CR (F)] most populated conformations.

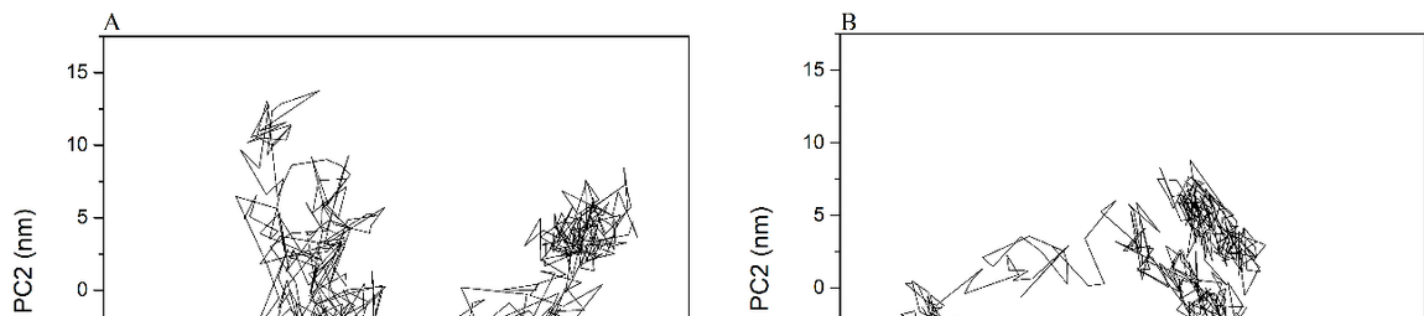


## Figure 4

Projection in phase space and FELs of the two systems. FELs as a function of the projection of PC1 and PC2 onto the essential subspace of the PPAR $\gamma$ -RXR $\alpha$  system (A) and the PPAR $\gamma$ -RXR $\alpha$ -DNA system (B). Projection of the motion in the phase space along the first and second eigenvectors (PC2 versus PC1) for the PPAR $\gamma$ -RXR $\alpha$  system (C) and the PPAR $\gamma$ -RXR $\alpha$ -DNA system (D). The color bar represents the relative free energy value in kJ/mol.